Improving carrier mobility in two-dimensional semiconductors with rippled materials

Hong Kuan Ng[1,2,#], Du Xiang[3,#], Ady Suwardi[1,4,#], Guangwei Hu[5], Ke Yang[6], Yunshan Zhao[7], Tao Liu[8], Zhonghan Cao[2], Huajun Liu[1], Shisheng Li[9], Jing Cao[1], Qiang Zhu[1], Zhaogang Dong[1,4], Chee Kiang Ivan Tan[1], Dongzhi Chi[1], Cheng-Wei Qiu[5], Kedar Hippalgaonkar[1,10], Goki Eda[2], Ming Yang[6,], Jing Wu[1,4,*]*

[1] Institute of Materials Research and Engineering, 2 Fusionopolis Way, Innovis, #08-03, Agency for Science, Technology and Research, Singapore

[2] Department of Physics, National University of Singapore, Singapore

[3] Frontier Institute of Chip and System, Fudan University, Shanghai 200438, China

[4] Department of Materials Science and Engineering, National University of Singapore, Singapore

[5] Department of Electrical and Computer Engineering, National University of Singapore, Singapore

[6] Department of Applied Physics, The Hong Kong Polytechnic University, Hong Kong

[7] NNU-SULI Thermal Energy Research Center (NSTER) & Center for Quantum Transport and Thermal Energy Science (CQTES), School of Physics and Technology, Nanjing Normal University, Nanjing, China

[8] Institute of Optoelectronics, Fudan University, Shanghai, China

[9] International Center for Young Scientists (ICYS), National Institute for Materials Science (NIMS), Tsukuba, Japan

[10] Department of Materials Science and Engineering, Nanyang Technological University, 50 Nanyang Avenue, 639798, Singapore

[#] These authors contributed equally to this work.

* Correspondence and requests for materials should be addressed to M. Y. (email: kevin.m.yang@polyu.edu.hk) or J. W. (email: wujing@imre.a-star.edu.sg)

This is the peer reviewed version of the following article: Ng H. K., et al, Improving carrier mobility in two-dimensional semiconductors with rippled materials, Nature Electronics, 5, 489–496, 2022, which has been published in final form at http://dx.doi.org/10.1038/s41928-022-00777-z.

Abstract:

Two-dimensional (2D) semiconductors could potentially replace silicon in future electronic devices. However, the low carrier mobility in 2D semiconductors at room temperature, caused by strong phonon scattering, remains a critical challenge. Here we show that lattice distortions can reduce electron-phonon scattering in 2D materials and thus improve charge carrier mobility. We introduce lattice distortions into 2D molybdenum disulfide (MoS_2) using bulged substrates, which create ripples in the 2D material leading to an enhancement in its dielectric constant. Consequently, a two orders of magnitude enhancement in room-temperature mobility is observed in the rippled-MoS_2 reaching $\sim 900\ \mathrm{cm^2\ V^{-1}\ s^{-1}}$, far exceeding the phonon-limited mobility of $\sim 410\ \mathrm{cm^2\ V^{-1}\ s^{-1}}$ in flat-MoS_2. We show that our approach can be used to create high-performance room-temperature field-effect transistors and thermoelectric devices.

Due to their atomically-thin nature, two-dimensional (2D) semiconductors such as transition metal dichalcogenides (TMDs) can potentially minimize the short channel effects that remain a key issue in advanced silicon-based transistors[1,2]. However, the use of 2D materials in electronics hinges on the development of large-scale, high quality growth methods, effective doping, high-*k* dielectric integration, ultralow contact resistance and high charge carrier mobility materials. Important advancements have been made in the growth of TMDs layers with chemical vapour deposition (CVD) methods[3–5], and recent breakthroughs show that contact resistance can be reduced using specialized integration processes or semi-metals[6–9]. However, the low room-temperature carrier mobility (μ) of 2D semiconductors remains a challenge toward applications for 2D electronics.

The underlying reason for the low carrier mobility in 2D semiconductors is strong phonon scattering. Several strategies have been developed to improve the carrier mobility of 2D semiconductors, including increasing dielectric screening using surrounding dielectrics[10,11], reducing scattering from impurities, traps, and defects by h-BN encapsulation[12,13], and reducing carrier effective mass by strain engineering[14,15]. Nevertheless, the phonon-limited transport at room-temperature in most stable 2D semiconductors still

limits mobility with values ranging between 10 and 100 $cm^2V^{-1}s^{-1}$, which are much smaller than conventional semiconductors such as silicon (μ~1400 cm^2 V^{-1} s^{-1}) and gallium arsenide (μ~8500 cm^2 V^{-1} s^{-1})[16,17].

Recently, enhancement beyond phonon-limited mobility was demonstrated in locally strained monolayer TMDs on substrates with high surface roughness[18], although the fundamental mechanism remains unclear. Strained 2D materials can also lead to unexpected phenomena such as flexoelectricity[19], suggesting unconventional pathways – lattice engineering, for instance – towards improved nanoelectronics. Theoretical analysis has suggested that the dielectric constant (ε) of materials could be an important parameter for identifying materials with high carrier mobility[20]. ε is an intrinsic material property characterizing the polarizability of the electron cloud to screen surrounding charges, which is a key factor determining charge mobility in the absence of phonon-limited scattering[21]. However, the value of ε depends on the periodic lattice potential of pristine materials, which has yet to be fully exploited to tailor intrinsic carrier mobility.

In this article, we show that charge carrier mobility in 2D MoS_2 can be enhanced by using substrates with bulged morphologies that induce ripples and thus lattice distortions in the MoS_2 layers. The lattice distortions create a larger electric polarization that can enhance intrinsic ε (ref. [16,17,22]) and renormalize the frequency of phonons. Consequently, the renormalized phonon frequency quenches the effective density of electron-phonon (E-P) scattering, which normally limits charge carrier mobility in conventional MoS_2 devices fabricated on flat substrates[23,24]. The enhanced intrinsic ε can then effectively screen polarized E-P interactions, whereas conventional dielectric screening by the surrounding media is only limited to small phonon momenta[25]. This way, the main carrier scattering mechanism shifts from E-P in flat MoS_2 (f-MoS_2) to charged-impurity (C-I) in rippled MoS_2 (r-MoS_2). Using our approach, we show that the room temperature carrier mobility of bilayer r-MoS_2 can be increased by two orders of magnitude, reaching values of ~$900\ \mathrm{cm^2V^{-1}s^{-1}}$. We also show that the high mobility in r-MoS_2 can be used to create high-performance in field-effect transistors (FET) and thermoelectric (TE) devices.

Rippled film formation and characterization

2D semiconductors easily conform to the local surface morphology owing to their flexibility (**Figure 1a**). Our MoS_2 flakes were mechanically exfoliated and transferred onto SiN_x/Si substrates with a bulged morphology (surface roughness $\delta z_{rms} = 2$ nm, **Figure 1b**) to obtain r-MoS_2 samples with the lattice distortion (highlighted in **Figure 1a)**. The conformation between MoS_2 and the bulged substrate is shown in cross-section TEM image (**Figure 1c**) and large-area AFM images **(Supplementary Fig. 1)**. **Figure 1d** shows the optical images of the transferred MoS_2 with monolayer, bilayer and trilayer thickness. The lattice distortion in r-MoS_2 can be observed in the red shift of the peak photoluminescence (PL) signal of monolayer r-MoS_2 (**Figure 1e**), consistent with earlier works[26]. However, it is worth noting that, this red shift by about 30 meV only represents an average strain induced in r-MoS_2 within the laser spot size (~ 1 μm). In fact, the local strain induced should be much larger depending on the height and width of the bulges as well as MoS_2 thickness, ranging between 0.1 % to 6 % (**Supplementary Fig. 13**). The effects of lattice distortion on the crystal structure and optical bandgap in r-MoS_2 (1-3 layers) are also probed using Raman spectroscopy. The comparison of Raman spectra between f-MoS_2 (SiO_2) and r-MoS_2 (SiN_x) (**Figure 1f**) shows that the E^1_{2g} (A_{1g}) mode due to *in-plane* (*out-of-plane*) vibration of Mo and S atoms at around 384 cm^{-1} (405 cm^{-1}) (ref. [27,28]), without Raman frequency shift, indicating the absence of global tensile and compressive strain. However, the intensity of both modes is quenched by about ten times in r-MoS_2 than that in f-MoS_2 regardless of the number of layers of MoS_2. These suggest weakened phonon vibrations due to the conformation between the MoS_2 flakes and the substrate, in which the induced strain field contributes lattice distortion and the quenching of phonon modes[26,29], as substantiated in our electronic transport measurement to be presented later. The quenching of phonon modes is also corroborated in our calculated phonon DOS (**Figure 1g**). For monolayer r-MoS_2 (under a curvature height of 1 Å, **Supplementary Fig. 2**), phonons have been renormalized due to lattice distortion induced by the bulged substrate. An increase in the frequency of acoustic phonons (inset of **Figure 1g**) and a renormalization of optical phonons were observed. This renormalization of optical phonons across a wider range of frequency weakens its intensity

due to the breaking of degeneracy induced by lattice distortion. The effect of renormalized phonons on mobility was revealed through the calculated effective density of scattering[17]. The renormalized phonons dramatically decrease the effective density of scattering in MoS_2 by one order of magnitude (**Figure 1h**), thus resulting in the strongly suppressed E-P scattering, especially for longitudinal acoustic (LA) due to strength of LA-electron scattering almost unchanging on substrate[30]. Although lattice distortion can affect the electronic structure of MoS_2, we found the slight change in electronic structure near the conduction band edge (such intra- and inter- valleys scattering) is not the dominating factor responsible for quenching electron-phonon scattering (**Supplementary Fig. 3c**).

Enhanced dielectric constant and FET performance

With quenched effective density of E-P scattering due to lattice distortion observed, we now discuss another fundamental property, i.e. the intrinsic ε of r-MoS_2, to fully understand the surprising electronic transport therein (**Figure 2a**). We perform first-principles calculation to obtain the static ε of monolayer and bilayer MoS_2 (**Figure 2b, Supplementary Fig. 4-6**). In this simulation, four idealized models are employed to study the effects of varied curvature on ε with curvature heights ranging from 0 to 4 Å. The calculated ε clearly shows that both the in-plane ($\varepsilon_{\parallel}$) and out-of-plane ($\varepsilon_{\perp}$) components significantly increases with curvature (and hence larger lattice distortion). This is attributed to the breaking of lattice symmetry that enables an enhanced electric polarization and thus a larger ε within r-MoS_2, which also agrees with our experimental ε measurement (**Supplementary Fig. 7-9**). We now discuss how the enhanced intrinsic ε could lead to large mobility in r-MoS_2. Typically, the increased electric polarization also increases scattering from polar-optical-phonons (Fröhlich interactions) at the working temperature of most electronic devices (near room temperature or above)[21,25], thus exacerbating carrier mobility instead. However, when phonons are heavily suppressed at the condition of, for example, low temperature[21,31], larger intrinsic ε actually guarantees the enhancement of mobility. In r-MoS_2 with lattice distortion, the renormalized phonon density and suppressed E-P scattering can be sustained (**Figure 2a**), therefore

allowing the boosted mobility at room temperature as a result of larger intrinsic ε. Specifically, the enhanced intrinsic ε is expected to screen Fröhlich interactions more effectively in r-MoS_2 at finite momenta, in contrast to external dielectric environment which only screens Fröhlich interactions in the limit of small phonon momenta[25]. Furthermore, considering both Fröhlich interactions and parabolic band structure at the band edge, the intrinsic carrier mobility is proportional to $\sim\varepsilon^2$ in the isotropic electron-phonon coupling approximation[20]. Thus, such high intrinsic ε simultaneously enables stronger dielectric screening and significantly enhances the intrinsic mobility ceilings of semiconductors[16,20].

We now experimentally showcase the impact of enhanced ε on charge transport via the two-probe transfer characteristics of monolayer r-MoS_2 on substrates with different surface roughness (**Figure 2c, Supplementary Figure 10**), where conductance and field effect carrier mobility (μ) exhibit rapid increase with increasing surface roughness (δz_{rms}). Irrespective of the flake thickness and device geometry, high values of μ are consistently achieved in r-MoS_2 across more than 120 devices with channel lengths ranging from 10 μm down to 200 nm (**Figure 2d & Supplementary Figure 14**). Our device exhibits two-probe FET mobility up to $646\ \mathrm{cm^2\ V^{-1}\ s^{-1}}$ in bilayer MoS_2. From drain characteristics, a linear relationship across a wide range of source-drain current and voltage ($I_{sd} - V_{sd}$) indicates ohmic contacts (**Figure 2e**). As larger V_{sd} is applied, the I_{sd} then saturates and plateaus, attaining an excellent saturation current density of $\sim300\ \mu\mathrm{A}\ \mu\mathrm{m}^{-1}$. These observations are counter-intuitive since roughness and surface defects are believed to intensify carrier scattering, thus degrading μ (ref. [12,13]). The μ values in r-MoS2 are even higher than its intrinsic phonon-limited mobility[23] as well as other studies (**Supplementary Table 1 & Supplementary Fig. 25**), thus suggesting that the improvement in μ is due to the enhanced ε of the material, as will be discussed later in details.

<u>Electrical transport and scattering mechanism</u>

Such observation is also agreeable with four-probe characterizations, in which case contact resistance effects are eliminated as a possible origin of the boosted μ (**Figure 3a, Supplementary Fig. 15-16**). **Figure**

3b shows room-temperature transfer characteristics of a bilayer r-MoS_2 device, which exhibited the highest μ among all our devices (**Supplementary Fig. 17**). We identify two regimes in the gate-dependent electrical conductivity σ: linear regime immediately above the threshold where the mobility peaks (blue-shaded region) and; sublinear regime where the mobility decreases gradually (red-shaded region). In the linear regime, μ reaches~ 900 $\mathrm{cm^2\ V^{-1} s^{-1}}$, up to two orders of magnitude larger than the typical bilayer MoS_2 on flat substrates (**Figure 3d**).

We now further examine the scattering mechanisms in r-MoS2 to better understand the effect of enhanced ε. Considering Drude model $\mu = q\tau/m^*$ where q is the elementary charge, τ is the carrier scattering time and m^* is the carrier effective mass, the large enhancement in μ cannot be attributed to m^*, since its reduction would be quite limited, as consistent with our thermoelectric characterization in the later section. In general, several scattering processes should be considered where each affects the μ in different ways, such as E-P scattering ($\tau_{E-P} \propto \varepsilon^0$), C-I scattering ($\tau_{C-I} \propto \varepsilon^2$) and carrier-carrier (C-C) scattering ($\tau_{C-C} \propto \varepsilon$). For non-phonon (N-P) scattering, τ is strongly dependent on ε, which can be approximately described using Matthiessen's rule as $1/\tau_{total} \approx 1/\tau_{N-P} = 1/\tau_{C-I} + 1/\tau_{C-C}$. However, C-C scattering is only prominent in samples with high carrier concentration or exceptionally low defect/impurity density[32]. Thus, transport in 2D semiconductors is usually dominated by phonons at high temperatures and by charged impurities at low temperatures. In this regard, C-C scattering plays a negligible role in r-MoS_2. Next, we measured the out-of-plane ε of r-MoS_2 (**Supplementary Fig. 8**), which is estimated to be $\varepsilon_{\perp} \sim 100$, more than an order of magnitude larger than that of f-MoS_2 (**Figure 3c**).

To determine the major scattering mechanisms in our r-MoS_2 devices, temperature dependence of the peak values of μ is investigated (**Figure 3d)**. Here, the overall trend is vastly different for r-MoS_2 and f-MoS_2. In f-MoS_2, μ increases with decreasing temperatures with power exponent $\gamma \sim 1.4$, which is typical for phonon-limited transport[10,13,23]. However, for r-MoS_2, μ mainly decreases with decreasing temperatures with $\gamma \sim -0.49$, which suggests the C-I dominated transport behavior in 2D systems[21]. At high temperatures ($T > 200$ K), the temperature exponent changes sign to $\gamma \sim 0.59$ for r-MoS_2, which is

unexpected for phonon-limited mobilities, thus implying the strongly suppressed E-P scattering at room temperature. This observation is consistent with the observed quenched Raman intensity as well as our calculations (**Figure 1d,f,g**). Unlike E-P scattering where μ is independent of ε, the scattering time τ_{C-I} in C-I transport is quadratically proportional to ε, i.e. $\tau_{C-I} \propto \varepsilon^2$ (ref. [32]). Given that the substrate-induced lattice distortion results in an order of magnitude enhancement in ε (**Figure 3c**), the ensuing dielectric screening towards long-range C-I scattering is successively enhanced. Thus, the C-I dominated μ in r-MoS_2 is expected to be up by two orders of magnitude, corroborated by our experimental observation. Therefore, for $-6 \leq V_g \leq 4$ V (blue-shaded region), C-I scattering is dominated by long-range Coulomb interactions where μ scales with ε^2. At higher gate regimes $V_g \geq 4$ V (red-shaded region), as more carriers are electrostatically injected, their electron cloud provides additional screening of the long-range Coulomb interactions. However, this instead amplifies short-range Coulomb scattering arising from the ripples which led to the decrease in μ (**Supplementary Figure**), consistent with our experimental observation (**Figure 3b**)[33,34]. Such a change in scattering mechanisms of r-MoS_2 can therefore explain the origin of the drastic two order of magnitude improvement in μ, consistent with the large increase in the ε of r-MoS_2 compared to f-MoS_2.

Nevertheless, changes to carrier concentration within r-MoS_2 may be one possibility that results in the observed enhancement in σ. To rule out such possibility, we measured transverse Hall resistance (R_{xy}) of r-MoS_2 as a function of magnetic field (B) at room temperature (**Figure 3e**). The change in carrier concentration (Δn_{2D}) as a function of V_g then directly gives the gate capacitance, $C_{\mathrm{Hall}} = 25\ \mathrm{nF\ cm^{-1}}$ (**Figure 3f**). This value agrees with capacitance extracted from field effect C_{FET} with $C_{\mathrm{Hall}}/C_{\mathrm{FET}} \cong 1.13$. Thus the σ enhancement is unlikely contributed by the carrier concentration. Therefore, the ultrahigh μ in r-MoS_2 is attributed to dominant C-I scattering, as evidenced by both the temperature dependence (γ) and dielectric constant dependence (ε) of μ.

<u>Thermoelectric performance</u>

With the origin of the anomalously high room-temperature mobility revealed, we next demonstrate their critical role for enhanced thermoelectric (TE) performance. The cornerstone to TE performance has always been the counter-balanced relationship between TE parameters: electrical conductivity (σ) and Seebeck coefficient (S). Mobility enhancement is commonly achieved to improve σ by either lowering m^* or increasing carrier concentration (n), which inevitably results in a compromised S, limiting the enhancement of TE power factor ($PF = S^2\sigma$) (ref. [35]). Here, we achieved high μ enhancement without changing n, such that the interdependency of TE parameters is significantly weakened. **Figure 4** shows the change of μ, σ, S, and PF as a function of electrostatically induced n in mono-, bi-, and trilayer r-MoS_2 and f-MoS_2 devices. The blue/red-shaded region is consistent with the two regimes in **Figure 3b.** At low carrier densities $n \cong 7 \times 10^{18}\ \mathrm{cm}^{-3}$, enhancement in μ leads to two orders of magnitude increase in σ for r-MoS_2. On the other hand, the corresponding reduction in S for r-MoS_2 is only $\sim 30\ \%$, which arises from strain with lowering m^* (ref. [15]) (**Figure 4c**). Since S is linearly proportional to m^*, the corresponding reduction in $m^*$is not expected to be the main contribution of the anomalously high μ (ref. [35]). Bi- and tri-layer r-MoS_2 exhibit higher S over the monolayer due to higher valley degeneracy and larger m^* (ref. [36,37]). Therefore, the resulting enhancement in PF is therefore not comprised by the reduced S (**Figure 4d**). The most distinct feature in r-MoS_2 is that such high μ enhancement is achieved without increasing n, which has not been reported so far. Hence, a high room temperature PF ($\geq 1\mathrm{mW\ m^{-1}\ K^{-2}}$) can be achieved at low doping levels ($n \sim 3 \times 10^{18}\ \mathrm{cm}^{-3}$), more than an order of magnitude higher than f-MoS_2. Such high PF at low n in r-MoS_2 also represents the highest values ever reported compared to other bulk and 2D systems (**Supplementary Fig. 18-20**).

Conclusion

We have shown that the intrinsic mobility limit of room-temperature charge transport in 2D semiconductors can be overcome by introducing ripples into the lattice structure of the material. Our simple and cost-effective approach can be used to create MoS_2 FET and TE devices with competitive room-

temperature performance and could potentially be used to create high mobility devices in a wide rangeo f 2D materials. processing. This work opens up a new frontier in designing ultra-high mobility devices in a wide range of 2D materials. The approach also harnesses the potential to be used in a broad range of electronic and optoelectronic devices, and the use of high-k dielectrics could further enhance device performance

Methods

Bulge SiN_x/Si substrates. Bulged SiN_x/Si substrates were purchased from Micro-Nano Research Materials Co., Ltd., which were grown by standard low pressure chemical vapor deposition (LPCVD) technique reported previously[38,39]. The density and height of bulges are tunable with pressure and reactant gas flow (SiH_4) during the LPCVD growth process, leading to the manipulation of granularity as well as surface roughness[40–42]. The as-grown SiN/Si bulged substrates are intrinsically and microscopically rough with δz_{RMS} of around 2 nm (Supplementary Figure 10) with a SiN_x layer thickness of about 300 nm (Supplementary Figure 11-12). Smaller δz_{RMS} can then be obtained by employing a wet polishing method (85 % phosphoric acid, 170 °C) to smoothen the bulges as shown in Supplementary Figure 10b,c,d,e. The relationship between δz_{RMS} and device mobility is shown in Figure 2c in the main manuscript. The chemical composition, purity, and uniformity of the SiN_x layer are confirmed using X-ray photoelectron spectroscopy (XPS) and ellipsometry measurements (Supplementary Figure 11-12).

Device Fabrication. 1L/2L/3L MoS_2 (HQ Graphene) were mechanically exfoliated onto polydimethylsiloxane (PDMS) and transferred onto 300 nm SiN_x/Si substrate. Other standard characterization tools include dimension FastScan Bruker atomic force microscopy to investigate the morphology and thickness of the samples. Electrodes were patterned by standard electron-beam lithography (FEI nanoSEM 230) process, followed by electron beam evaporation (AJA ATC-Orion-8E-UHV) of titanium/gold (Ti/Au) of 5/65 nm for large electrodes and gold (Au) of 50 nm for small electrodes. A total

of 126 r-MoS_2 devices and 3 f-MoS_2 devices of different thicknesses are measured in this work. Device channel lengths: 200 nm to 10 μm; channel width: 500 nm to 2 μm. Electrical characterizations shown in **Figure 2** and **Supplementary Fig. 14** are based on the selected representative morphologies of the substrates.

Transport Measurements. 4-probe measurements were employed to eliminate contact resistance and extract a precise electrical conductivity of the r-MoS_2 flakes for different gate voltages (Supplementary Fig. 16). The temperature-dependent mobility was extracted from transfer characteristics, via $\mu = \frac{dI_{sd}}{dV_g} \cdot \frac{1}{V_{sd}} \cdot \frac{1}{C_{ox}} \cdot \frac{L}{W}$, where $C_{ox} = 22\ \mathrm{nF\ cm^{-2}}$ is the capacitance for $300\ \mathrm{nm}$ thick SiN_x. The electrical conductivity ($\sigma = \frac{L}{W \cdot t} \cdot G$) was calculated from G by considering the device geometry: length (L), width (W), thickness (t) and conductance (G). To measure Seebeck coefficient $S = \frac{V_s}{\Delta T}$, a temperature gradient along the sample was realized Joule heating by applying a DC current bias (I) through a metal microheater using a source-meter (Keithley 6221). The temperature gradient generates the thermoelectric open-circuit voltage (V_s), which was measured by a voltmeter (Keithley 6430). As a series of DC current bias is applied to the microheater, their corresponding V_s were recorded. The temperature gradient is calibrated using the 4-probe resistance of thermometers (Supplementary Fig. 22-24).

First-principles calculations. All the first-principles calculations were performed by using density-functional theory based Vienna Ab initio Simulation Package (VASP.6.2.0) (ref. [43]), in which the Perdew–Burke–Ernzerhof (PBE) (ref. [44]) form of the generalized gradient approximation (GGA) were used for the exchange-correlation functionals and projector augmented-wave (PAW) (ref. [45]) method was applied for the interaction between valence electrons and ion cores. For all the calculations, the cut-off energy for the plane wave expansion was set to 500 eV. In this study, we have considered four idealized model structures based on monolayer and bilayer MoS_2: the flat MoS_2 $(3\sqrt{3} \times 1)$ supercell, and the MoS_2 $(4\sqrt{3} \times 1)$

supercells with a curvature height of 2 Å, 3 Å and 4 Å, respectively, in which the curvatures were induced by bending the monolayer and bilayer MoS_2 supercells with the sine function distribution along the armchair direction. In these models, the thickness of vacuum layer was set to 30 Å and normal to MoS_2 basal plane. The Γ-centred 15×15×1 and 3×15×1 k-point meshes were used for bilayer MoS_2 unit cell and supercells. The energy and force on each atom were converged to be less than 1×10^{-8} eV and 1×10^{-8} eV/Å, respectively. Van der Waals correction in the bilayer MoS_2 was included using the method of Grimme (DFT-D3) (ref. [46]). The frequency dependent dielectric matrix was calculated using the independent-particle approximation[47], in which more than 60 empty bands per atom were included. We also employed the finite displacement method to calculate the phonon density of states for both monolayer r-MoS_2 and f-MoS_2 supercells using Phonopy code[48]. The effective density of electron-phonon scattering at each K point was calculated by $D(i\boldsymbol{k}) = \sum_{j,i'} \int \frac{d\boldsymbol{q}}{\Omega_{BZ}} C_{i\boldsymbol{k},i'\boldsymbol{k}',j\boldsymbol{q}}$, which is defined by Cheng *et al*. (ref. [17]). The

$i\boldsymbol{k}$ to $i'\boldsymbol{k}'$ and $j\boldsymbol{q}$initial electronic state, the final electronic state, and the absorbed or emitted phonon, respectively. The Ω_{BZ} is area of the Brillouin zone, which is set to 1 due to same cell in our calculation. and $C_{i\boldsymbol{k},i'\boldsymbol{k}',j\boldsymbol{q}}$ is the number of phonons that can scatter the electronic state from $i\boldsymbol{k}$ to $i'\boldsymbol{k}'$(energy and momentum conservation should be considered). The dense Γ-centred 50×200×1 k-point and 50×200×1 q-point meshes were used to calculate the electronic and phonon structures.

Data availability

All data generated or analyzed during this study are included in the published article and its Supplementary Information. Source data are provided with this paper.

References

1. Wang, Q. H., Kalantar-Zadeh, K., Kis, A., Coleman, J. N. & Strano, M. S. Electronics and optoelectronics of two-dimensional transition metal dichalcogenides. *Nat. Nanotechnol.* **7**, 699–712 (2012).
2. Chhowalla, M., Jena, D. & Zhang, H. Two-dimensional semiconductors for transistors. *Nat. Rev. Mater.* **1**, 16052 (2016).
3. Zhou, J. *et al.* A library of atomically thin metal chalcogenides. *Nature* **556**, 355–359 (2018).
4. Aljarb, A. *et al.* Ledge-directed epitaxy of continuously self-aligned single-crystalline nanoribbons of transition metal dichalcogenides. *Nat. Mater.* **19**, 1300–1306 (2020).
5. Edelberg, D. *et al.* Approaching the Intrinsic Limit in Transition Metal Diselenides via Point Defect Control. *Nano Lett.* **19**, 4371–4379 (2019).
6. Shen, P. C. *et al.* Ultralow contact resistance between semimetal and monolayer semiconductors. *Nature* **593**, 211–217 (2021).
7. Wang, Y. *et al.* Van der Waals contacts between three-dimensional metals and two-dimensional semiconductors. *Nature* **568**, 70–74 (2019).
8. Liu, Y. *et al.* Approaching the Schottky-Mott limit in Waals metal – semiconductor junctions. *Nature* **557**, 696–700 (2018).
9. Chai, J. W. *et al.* Tuning Contact Barrier Height between Metals and MoS2 Monolayer through Interface Engineering. *Adv. Mater. Interfaces* **4**, 1–8 (2017).
10. Radisavljevic, B. & Kis, A. Mobility Engineering and a Metal-insulator Transition in Monolayer MoS2. *Nat. Mater.* **12**, 815–820 (2013).
11. Yu, Z. *et al.* Realization of Room-Temperature Phonon-Limited Carrier Transport in Monolayer MoS2 by Dielectric and Carrier Screening. *Adv. Mater.* **28**, 547–552 (2016).
12. Dean, C. R. *et al.* Boron nitride substrates for high-quality graphene electronics. *Nat. Nanotechnol.* **5**, 722–726 (2010).

13. Cui, X. *et al.* Multi-terminal transport measurements of MoS2 using a van der Waals heterostructure device platform. *Nat. Nanotechnol.* **10**, 534–540 (2015).
14. Lloyd, D. *et al.* Band Gap Engineering with Ultralarge Biaxial Strains in Suspended Monolayer MoS2. *Nano Lett.* **16**, 5836–5841 (2016).
15. Hosseini, M., Elahi, M., Pourfath, M. & Esseni, D. Strain-induced modulation of electron mobility in single-layer transition metal dichalcogenides MX2 (M = Mo, W; X = S, Se). *IEEE Trans. Electron Devices* **62**, 3192–3198 (2015).
16. Cheng, L. & Liu, Y. What Limits the Intrinsic Mobility of Electrons and Holes in Two Dimensional Metal Dichalcogenides? *J. Am. Chem. Soc.* **140**, 17895–17900 (2018).
17. Cheng, L., Zhang, C. & Liu, Y. Why Two-Dimensional Semiconductors Generally Have Low Electron Mobility. *Phys. Rev. Lett.* **125**, 177701 (2020).
18. Liu, T. *et al.* Crested two-dimensional transistors. *Nat. Nanotechnol.* **14**, 223–226 (2019).
19. Zhuang, X., He, B., Javvaji, B. & Park, H. S. Intrinsic bending flexoelectric constants in two-dimensional materials. *Phys. Rev. B* **99**, 054105 (2019).
20. He, X., Singh, D. J., Boon-on, P., Lee, M. & Zhang, L. Dielectric Behavior as a Screen in Rational Searches for Electronic Materials: Metal Pnictide Sulfosalts. *J. Am. Chem. Soc.* **140**, 18058–18065 (2018).
21. Ma, N. & Jena, D. Charge Scattering and Mobility in Atomically Thin Semiconductors. *Phys. Rev. X* **4**, 11043 (2013).
22. Kumar, A. & Ahluwalia, P. K. Mechanical strain dependent electronic and dielectric properties of two-dimensional honeycomb structures of MoX2 (X=S, Se, Te). *Phys. B Condens. Matter* **419**, 66–75 (2013).
23. Kaasbjerg, K., Thygesen, K. S. & Jacobsen, K. W. Phonon-limited mobility in n-type single-layer MoS 2 from first principles. *Phys. Rev. B* **85**, 115317 (2012).
24. Yu, Z. *et al.* Analyzing the Carrier Mobility in Transition-Metal Dichalcogenide MoS2 Field-Effect Transistors. *Adv. Funct. Mater.* **27**, 1604093 (2017).

25. Sohier, T., Calandra, M. & Mauri, F. Two-dimensional Fröhlich interaction in transition-metal dichalcogenide monolayers: Theoretical modeling and first-principles calculations. *Phys. Rev. B* **94**, 085415 (2016).

26. Conley, H. J. *et al.* Bandgap engineering of strained monolayer and bilayer MoS2. *Nano Lett.* **13**, 3626–3630 (2013).

27. Zhang, X. *et al.* Phonon and Raman scattering of two-dimensional transition metal dichalcogenides from monolayer, multilayer to bulk material. *Chem. Soc. Rev.* **44**, 2757–2785 (2015).

28. Li, H. *et al.* From bulk to monolayer MoS2: Evolution of Raman scattering. *Adv. Funct. Mater.* **22**, 1385–1390 (2012).

29. Jiang, J. W., Park, H. S. & Rabczuk, T. Molecular dynamics simulations of single-layer molybdenum disulphide (MoS2): Stillinger-Weber parametrization, mechanical properties, and thermal conductivity. *J. Appl. Phys.* **114**, 064307 (2013).

30. Zhang, C., Cheng, L. & Liu, Y. Role of flexural phonons in carrier mobility of two-dimensional semiconductors: free standing vs on substrate. *J. Phys. Condens. Matter* **33**, (2021).

31. Yang, F. *et al.* Gate-Tunable Polar Optical Phonon to Piezoelectric Scattering in Few-Layer Bi2O2Se for High-Performance Thermoelectrics. *Adv. Mater.* **33**, 2004786 (2021).

32. Lundstrom, M. *Fundamentals of Carrier Transport*. *Cambridge University Press* (Cambridge University Press, 2000). doi:https://doi.org/10.1017/CBO9780511618611.

33. Das Sarma, S., Adam, S., Hwang, E. H. & Rossi, E. Electronic transport in two-dimensional graphene. *Rev. Mod. Phys.* **83**, 407–470 (2011).

34. Tracy, L. A. *et al.* Observation of percolation-induced two-dimensional metal-insulator transition in a Si MOSFET. *Phys. Rev. B* **79**, 1–6 (2009).

35. Wu, J., Chen, Y., Wu, J. & Hippalgaonkar, K. Perspectives on Thermoelectricity in Layered and 2D Materials. *Adv. Electron. Mater.* **4**, 1800248 (2018).

36. Hippalgaonkar, K. *et al.* High thermoelectric power factor in two-dimensional crystals of MoS2.

Phys. Rev. B **95**, 115407 (2017).

37. Ng, H. K., Chi, D. & Hippalgaonkar, K. Effect of dimensionality on thermoelectric powerfactor of molybdenum disulfide. *J. Appl. Phys.* **121**, 204303 (2017).
38. Olson, J. M. Analysis of LPCVD process conditions for the deposition of low stress silicon nitride. Part I: preliminary LPCVD experiments. *Mater. Sci. Semicond. Process.* **5**, 51–60 (2002).
39. Yang, C. & Pham, J. Characteristic Study of Silicon Nitride Films Deposited by LPCVD and PECVD. *Silicon* **10**, 2561–2567 (2018).
40. Liu, X. J. *et al.* Growth and properties of silicon nitride films prepared by low pressure chemical vapor deposition using trichlorosilane and ammonia. *Thin Solid Films* **460**, 72–77 (2004).
41. Liu, X.-J., Jin, C.-Y., Zhang, J.-J., Huang, Z.-Y. & Huang, L.-P. Growth Rate and Surface Morphology of Silicon Nitride Thin Films by Low Pressure Chemical Vapor Deposition. *J. Inorg. Mater.* **19**, (2004).
42. Tonnberg, S. Optimisation and characterisation of LPCVD silicon nitride thin film growth. *Chalmers Open Digital Repository* (Chalmers University of Technology, 2006).
43. Kresse, G. & Furthmüller, J. Efficient iterative schemes for ab initio total-energy calculations using a plane-wave basis set. *Phys. Rev. B* **54**, 11169–11186 (1996).
44. Perdew, J. P., Burke, K. & Ernzerhof, M. Generalized gradient approximation made simple. *Phys. Rev. Lett.* **77**, 3865–3868 (1996).
45. Blöchl, P. E. Projector augmented-wave method. *Phys. Rev. B* **50**, 17953–17979 (1994).
46. Grimme, S. Semiempirical GGA-Type Density Functional Constructed with a Long-Range Dispersion Correction. *J. Comput. Chem.* **27**, 1787–1799 (2006).
47. Souza, I., Íñiguez, J. & Vanderbilt, D. First-Principles Approach to Insulators in Finite Electric Fields. *Phys. Rev. Lett.* **89**, 9–12 (2002).
48. Togo, A. & Tanaka, I. First principles phonon calculations in materials science. *Scr. Mater.* **108**, 1–5 (2015).

Acknowledgements

J. W. acknowledges the SERC Central Research Fund (CRF: KIMR211001kSERCRF) and Advanced Manufacturing and Engineering Young Individual Research Grant (AME YIRG Grant No.: A2084c170). D. C. and J. W. acknowledge National Research Foundation Competitive Research Programs (NRFCRP24-2020-0002). M.Y. acknowledges the funding support (project ID: 1-BE47) from The Hong Kong Polytechnic University. K.H. acknowledges funding from the Accelerated Materials Development for Manufacturing Program at A*STAR via the AME Programmatic Fund by the Agency for Science, Technology and Research under Grant No. A1898b0043. We acknowledge Centre for Advanced 2D Materials and Graphene Research at National University of Singapore.

Author contributions

J. W. conceived the idea of the experiments and design the project. J. W. and M. Y. supervised the project. H.-K. N. and D. X. prepared substrates and fabricated devices. J. W., H.-K. N., D. X., and T. L. performed electrical transport characterization. M. Y. and K. Y. conducted first-principles calculations. Data analysis and interpretations were carried out by J. W., M. Y., H.-K. N., A. S., G. H., C. -W. Q., K. H., G. E. and all other co-authors. H.-K.N., J. W. A. S., M. Y., G. H. and C. -W. Q., initiated the draft with inputs and comments from all authors. All authors discussed the results and provided constructive comments on the manuscript.

Competing interests

The authors declare no competing interests.

Additional information

Supplementary information The online version contains supplementary information available at

Correspondence and requests for materials should be addressed to M.Y. or J.W.

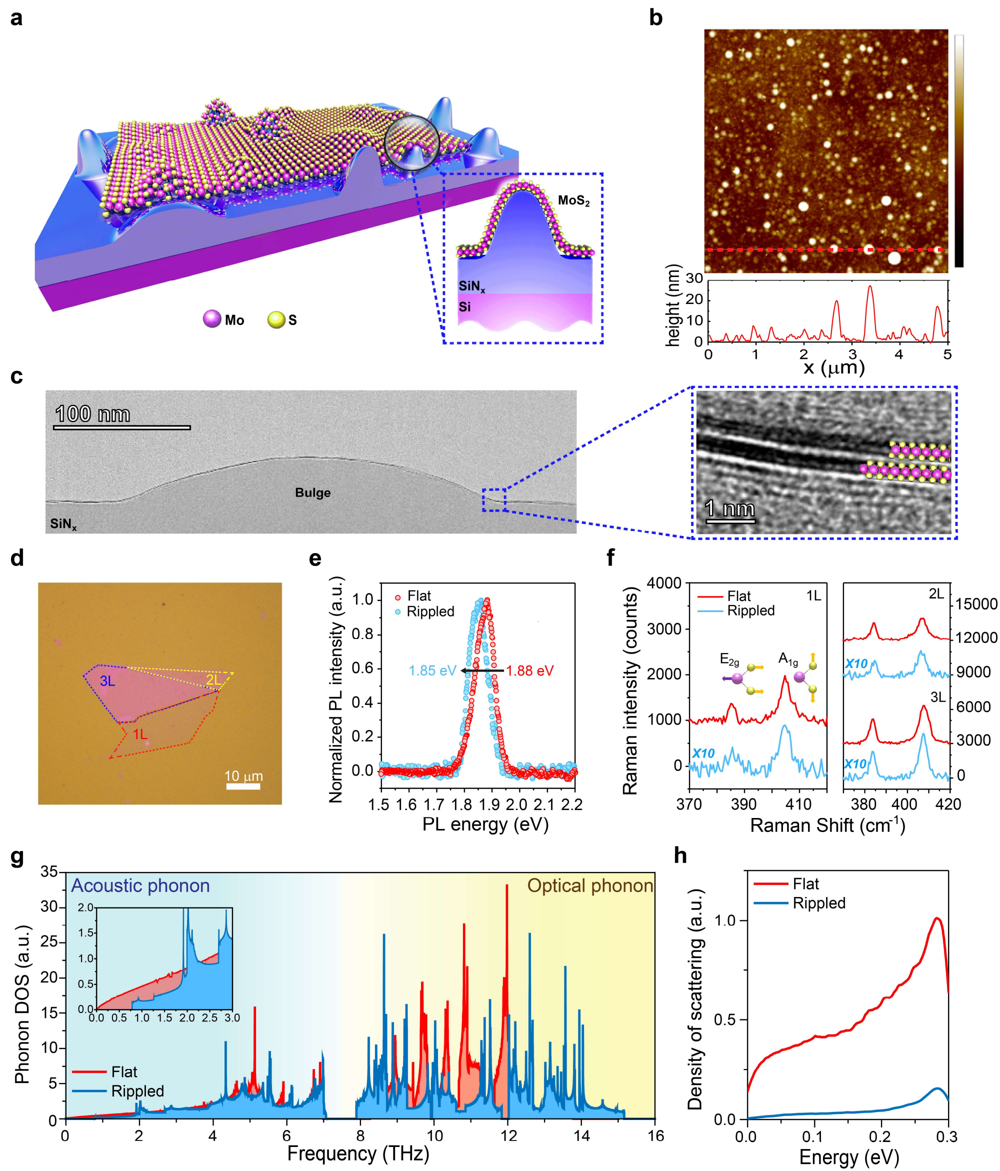

Fig. 1 | Material characterization and phonon DOS in f-MoS_2 and r-MoS_2. **a**, Illustration of monolayer r-MoS_2, where the conformation between MoS_2 and the bulged substrate is shown in the inset. **b**, AFM image of the bulged substrate with a root-mean-square (rms) surface roughness of $\delta z_{rms} = 2$ nm. **c**, Cross-section TEM image showing excellent conformation between MoS_2 and the bulged substrate. **d**, Optical microscope image of r-MoS_2 with thicknesses outlined: monolayer (red), bilayer (yellow), trilayer (blue). **e**, Normalized photoluminescence spectra of monolayer f-MoS_2 and r-MoS_2, averaged within a laser spot size of 1 μm. **f**, Raman spectra comparing f-MoS_2 and r-MoS_2 show quenched in-plane (E_{2g}) and out-of-plane (A_{1g}) vibration modes. **g**, Calculated phonon DOS in f-MoS_2 and in r-MoS_2 (under curvature height of 1 Å), with frequencies of acoustic (optical) phonons shaded in blue (yellow) background. **h**, Effective density of electron-phonon scattering as a function of electronic energy.

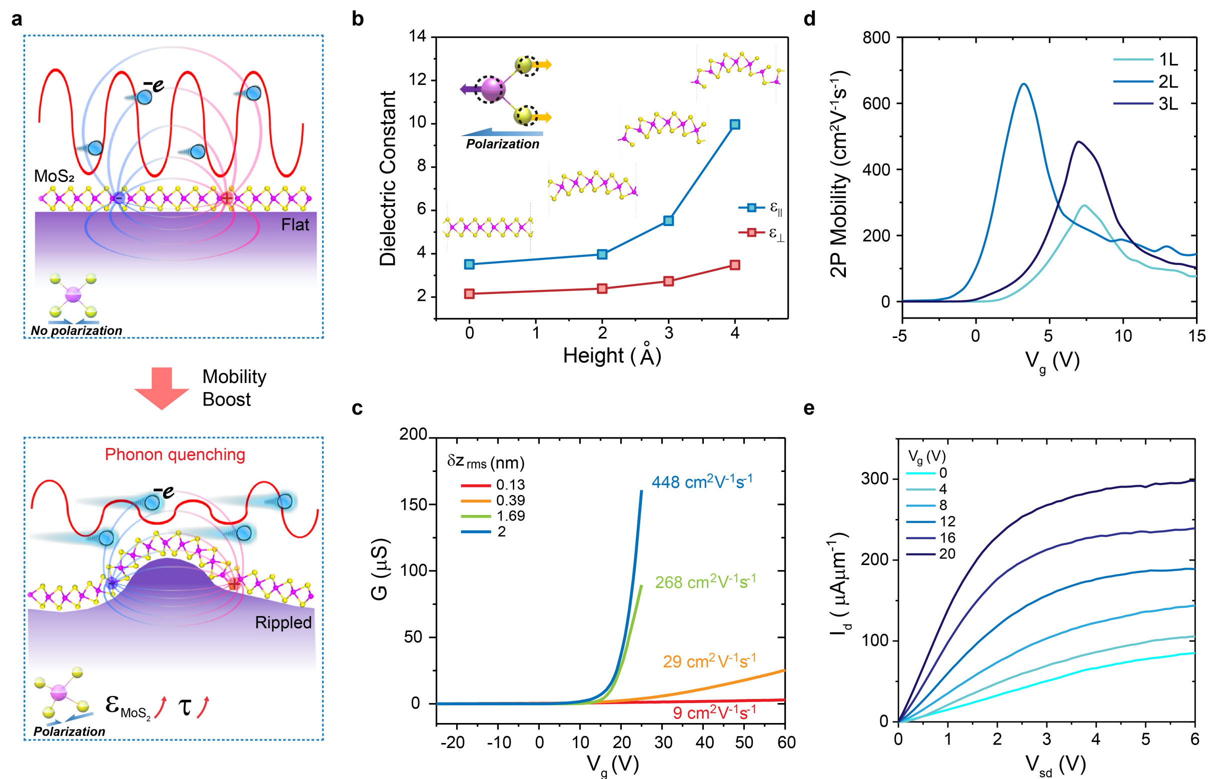

Fig. 2 | Transport mechanism and enhanced dielectric constant and FET performance in r-MoS2. a, Illustration of f-MoS2 and r-MoS2. The substrate-induced lattice distortion in r-MoS2 results in an increased electric polarization which enhances intrinsic dielectric constant (ε) to improve dielectric screening and concurrently quenches E-P scattering. This leads to drastically boosted carrier mobility. Electric field lines between positive and negative charges depict the strength of dielectric screening. Red solid lines represent phonon vibrations. Pink and yellow spheres represent Mo and S atoms, respectively. The change in electric polarization within f-MoS2 and r-MoS2 is also depicted. **b**, Illustration of monolayer MoS2 with four varying curvatures employed for first-principles calculations, and the calculated static dielectric constants (in-plane, $\varepsilon_{\parallel}$ and out-of-plane, $\varepsilon_{\perp}$) for different curvature heights. **c**, Two-probe FET transfer characteristics of monolayer r-MoS2 with increasing rms surface roughness (δz_{rms}), labelled with their respective carrier mobility. The increase in δz_{rms} results in larger lattice distortion hence higher ε leading to enhanced mobility. V_{sd} = 50 mV. **d**, Two-probe FET mobility of mono-, bi-, and tri-layer r-MoS2 as a function of gate voltage. **e**, Drain characteristics of monolayer r-MoS2 for different gate voltages (V_g).

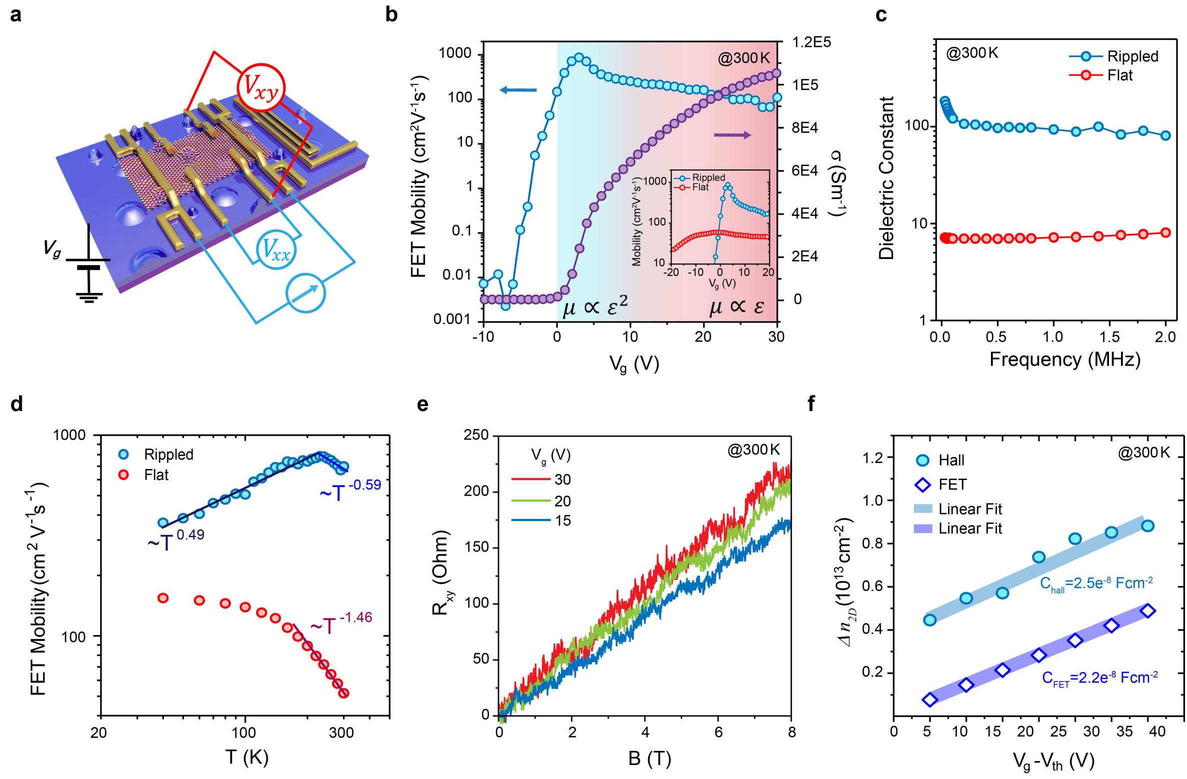

Fig. 3 | Transport measurements of bilayer r-MoS₂. a, Illustration of r-MoS₂ device structure which allows four-probe and Hall characterization. **b**, Four-probe FET mobility and electrical conductivity of r-MoS₂ as a function of backgate voltage at 300K. Charge scattering in r-MoS₂ can be mainly described as $1/\tau_{total} = 1/\tau_{C-I} + 1/\tau_{C-C}$ owing to the enhanced dielectric screening and suppression of E-P scattering. Blue-shaded region represents the linear regime immediately above the threshold where mobility peaks and exhibits a quadratic dependence due to dominant C-I scattering ($\mu \propto \tau_{C-I} \propto \varepsilon^2$), while the red-shaded region represents the sublinear regime where mobility decreases gradually due to higher carrier density ($\mu \propto \tau_{C-C} \propto \varepsilon$). Inset: Comparison of mobility as a function gating between r-MoS₂ and f-MoS₂) **c**, Out-of-plane dielectric constant ($\varepsilon_{\perp}$) of r-MoS₂ and f-MoS₂ as a function of frequency, extracted from ε measurements (Supplementary Fig. 5 and 6). **d**, Peak values of FET mobility as a function of temperature fitted with the power law $\mu \sim T^{-\gamma}$ where dominant C-I (E-P) scattering transport are observed in r-MoS₂ (f-MoS₂). **e**, Transverse Hall resistance (R_{xy}) of r-MoS₂ as a function of magnetic field (B) at different V_g at 300 K. **f**, Comparison of the change in carrier concentrations between Hall and FET measurement. The extracted capacitance from Hall measurement is consistent with the substrate capacitance.

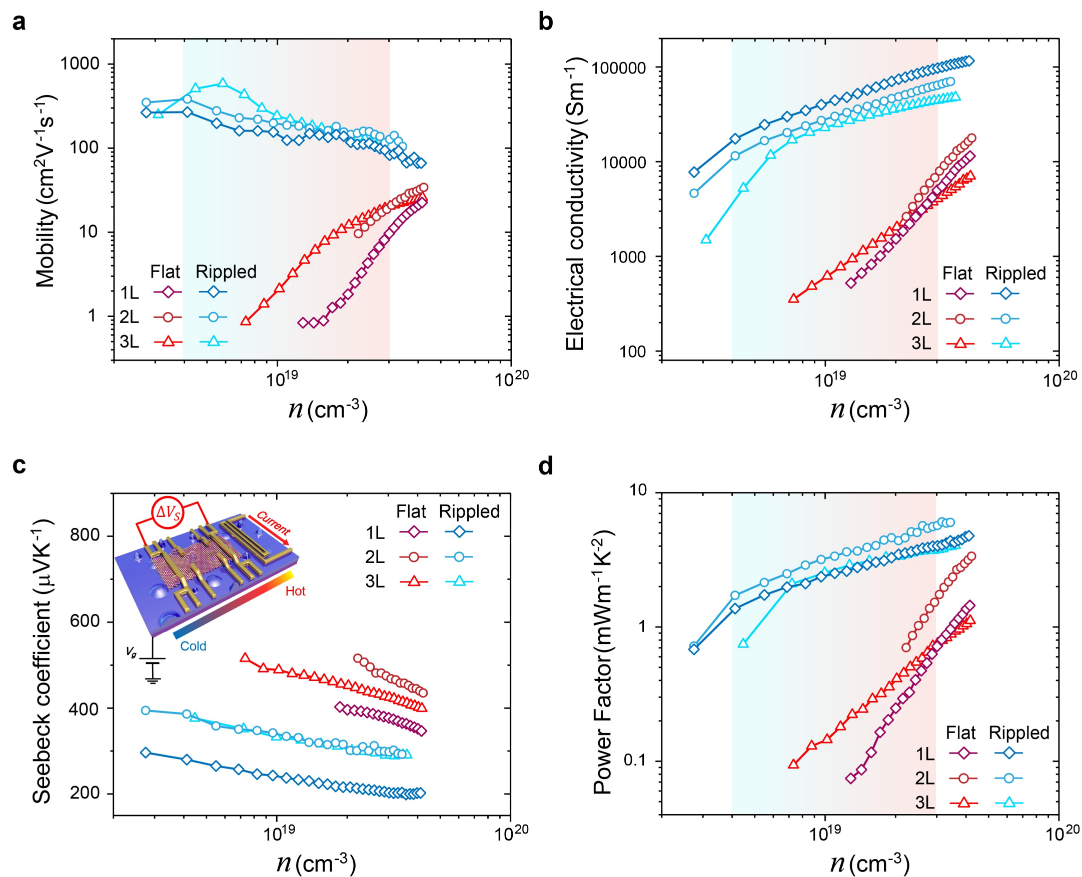

Fig. 4 | Thermoelectric properties of 1L/2L/3L r-MoS_2 (blue) and f-MoS_2 (red) as a function of carrier concentration (n) at 300 K. a, Mobility; **b**, Electrical conductivity; **c**, Seebeck coefficient; and **d**, Power factor. The blue-shaded region represents dominant C-I scattering regime, highlighting the drastic enhancement in mobility that leads to a significantly enhanced σ. With increasing carrier concentration, mobility gradually reduces as more carriers are electrostatically injected, indicated by the red-shaded region. This trend is similarly reflected in *PF*. The small reduction in S is attributed to the reduction of carrier effective mass (m^*) originating from substrate-induced lattice distortion. Inset in **c** illustrates the measurement of the Seebeck open-circuit voltage. Collectively, the manifestation of ultra-high mobility effectively decouples the interdependencies between σ and S thus leading to large enhancement in *PF* in all measured carrier concentration range.